Effects of bulk and interfacial anharmonicity on thermal conductance at solid/solid interfaces

Nam Q. Le, Carlos A. Polanco, Rouzbeh Rastgarkafshgarkolaei, Jingjie Zhang, Avik W. Ghosh, and Pamela M. Norris

Phys. Rev. B **95**, 245417 — Published 16 June 2017

DOI: 10.1103/PhysRevB.95.245417

Effects of bulk and interfacial anharmonicity on thermal conductance at solid/solid interfaces

Nam Q. Le,[1,*] Carlos A. Polanco,[2] Rouzbeh Rastgarkafshgarkolaei,[1]
Jingjie Zhang,[2] Avik W. Ghosh,[2,3] and Pamela M. Norris[1,†]

[1]*Department of Mechanical and Aerospace Engineering, University of Virginia, Charlottesville, Virginia 22904*

[2]*Department of Electrical and Computer Engineering, University of Virginia, Charlottesville, Virginia 22904*

[3]*Department of Physics, University of Virginia, Charlottesville, Virginia 22904*

(Dated: May 24, 2017)

Abstract

We present the results of classical molecular dynamics simulations to assess the relative contributions to interfacial thermal conductance from inelastic phonon processes at the interface and in the adjacent bulk materials. The simulated system is the prototypical interface between argon and "heavy argon" crystals, which enables comparison with many past computational studies. We run simulations interchanging the Lennard-Jones potential with its harmonic approximation to test the effect of anharmonicity on conductance. The results confirm that the presence of anharmonicity is correlated with increasing thermal conductance with temperature, which supports conclusions from prior experimental and theoretical work. However, in the model Ar/heavy-Ar system, anharmonic effects at the interface itself contribute a surprisingly small part of the total thermal conductance. The larger fraction of the thermal conductance at high temperatures arises from anharmonic effects away from the interface. These observations are supported by comparisons of the spectral energy density, which suggest that bulk anharmonic processes increase interfacial conductance by thermalizing energy from modes with low transmission to modes with high transmission.

I. INTRODUCTION

The contribution of inelastic phonon processes to the thermal conductance at solid/solid interfaces is a topic of enduring interest. At interfaces between metal films and dielectric substrates whose phonon spectra are extremely mismatched—e.g., Pb/diamond—experimentally measured values can far exceed the phonon radiation limit,[1–4] which represents the upper limit of conductance when accounting only for elastic (i.e., frequency-preserving) phonon transmission. The measured values also increase monotonically with temperature, in common with calculations of conductance from molecular dynamics (MD) simulations which naturally include anharmonic effects.[5–7] These observations strongly suggest that inelastic scattering (i.e., energy transfer among modes of different frequency) contribute a large fraction of conductance at high temperature. Since inelastic processes arise from anharmonicity of interatomic forces, the contribution is also expected to grow as temperature (and hence atomic displacement) increases, making it relevant to thermal engineering in applications with high operating temperatures such as high-power electronics.[8–10]

The seminal models for predicting conductance, the acoustic mismatch model[11,12] and diffuse mismatch model (DMM),[13,14] only account for elastic transmission processes. Only elastic processes are expected in a system with harmonic interatomic forces or, alternatively, in an anharmonic system under small displacements. Under this assumption, the DMM provides a first approximation for estimating the conductance. Based on comparison with experimental data, the DMM appears to generally overestimate the conductance between vibrationally well-matched materials and underestimate the conductance between mismatched materials.[15] The degree of matching is often summarized in the ratio of Debye temperatures, θ_D, and the transition between these two regimes is observed empirically when θ_D of the substrate is $\sim$3–4 times that of the film.[15] For example, lead and diamond have an extraordinarily high mismatch in vibrational spectra: the highest-frequency phonons in Pb are $\sim$2.2 THz, while those in diamond are $\sim$39.2 THz.[16,17] The expected conductance due only to *elastic* phonon transmission is correspondingly low, on the order of 2 MW m^{-2} K^{-1}. However, this underestimates experimental measurements by a full order of magnitude, with reported values ranging roughly 20–60 MW m^{-2} K^{-1}.[2–4]

Several modifications to the DMM have been proposed to account for inelastic transmission processes in predictions of conductance.[18–22] For example, Hopkins and coworkers proposed two modifications to the DMM: the higher harmonic inelastic model (HHIM)[20] and the anharmonic

inelastic model (AIM)[21] which provide expressions for the transmissivities corresponding to n-phonon processes: $\omega_1 + \omega_2 + \cdots + \omega_{n-1} \leftrightarrow \omega_n$, where ω denotes phonon frequency. By comparison an elastic (2-phonon) process would be denoted $\omega \rightarrow \omega$. The HHIM only allows processes that combine phonons of equal frequency ($\omega_1 = \cdots = \omega_{n-1}$), while the AIM allows the combination of phonons of arbitrary frequency. Duda and coworkers also proposed a modification to the DMM that incorporates bulk-like scattering near the interface rather than at the interface itself, which they used to predict an increasing conductance with temperature in the classical limit.[22] Despite making different assumptions about the details of inelastic processes, these models improve agreement with conductance measurements to similar degrees, making it difficult to determine their relative validity.

Several recent works have elucidated the details of inelastic processes and their contributions to thermal conductance. The theoretical and computational work by Sääskilahti et al.[7] showed that frequency-doubling and -halving processes dominate the inelastic contribution to conductance in MD simulations, lending support to the assumptions of the HHIM. However, Hohensee et al.[4] observed experimentally that the conductance of metal/diamond interfaces depends only weakly on pressure, from which they inferred that inelastic processes involving two metal phonons of equal frequency cannot be the dominant contribution to the conductance. Both works observed that their conclusions may be reconciled by careful consideration of the inelastic processes in the bulk-like regions near the interface. This precise question was investigated in Refs. 23 and 24. Using MD, Wu and Luo[23] simulated the conductance between one crystal with a monatomic basis and another crystal with a diatomic basis. They observed that increasing an anharmonic force constant in the diatomic lattice increased the total conductance dramatically due to increased coupling between acoustic and optical modes. By contrast, increasing an anharmonic force constant of the interfacial interaction had no effect on the conductance. This is broadly consistent with our results, but differs with our observation that the interfacial contribution is significant (though smaller than the bulk contribution). Furthermore, the present results expand on how the relative contributions change with temperature. A related difference is that size effects were observed, which did not affect their qualitative conclusions but precluded the quantitative comparison of the contributions from elastic, bulk inelastic, and interfacial inelastic processes. Nevertheless, we observe the same general mechanism that Wuo and Luo identified: inelastic processes contribute to conductance via the bulk thermalization of modes with low transmissivity. In a different work, Murakami et al.[24] made related conclusions from MD simulations of PbTe/PbS and Si/Ge interfaces, in which

they demonstrated the importance of inelastic processes in a broad transition region (TR) rather than only at the plane of the interface. Inelastic processes in the TR downconvert energy from high-frequency to low-frequency modes, which then transmit elastically, in agreement with our observations. However, their analysis did not provide a direct calculation of the separate elastic and inelastic contributions to conductance, nor the temperature dependence of the contributions, which will be essential for testing models that correctly incorporate inelastic processes.

Therefore, the goal of the present work is to decompose the thermal conductance at a model interface into explicit contributions from the harmonic dynamics, the anharmonic effects at the interface, and the anharmonic effects in the bulk materials. Our model system is a planar interface between Ar and "heavy Ar," which has been the prototypical model system for studying these phenomena. In Sec. II we present calculations of the conductance in the model system with different configurations of harmonic and anharmonic forces between atoms. The results confirm that conductance rises with temperature only in the systems with anharmonic forces, which presumably enable inelastic phonon processes. However, at high temperatures, the anharmonicity at the interface itself appears to contribute less than half of the total conductance in our model system; the anharmonicity in the bulk materials is responsible for the rest. These observations are corroborated in Sec. III, in which use the wavelet transform to calculate the spectral energy densities throughout the interfacial systems. Those spectra show that energy reflected from the interface is in strong non-equilibrium, and anharmonicity enables its thermalization, suggesting a mechanism to explain the increase in interfacial conductance. We summarize the findings in Sec. IV and comment on their relation to other research on this topic.

II. EFFECT OF LOCAL ANHARMONICITY ON INTERFACIAL THERMAL CONDUCTANCE

In this section, we present calculations of interfacial thermal conductance using non-equilibrium molecular dynamics (NEMD). Further simulation details are given in Appendix A. As a prototypical anharmonic potential, we use the Lennard-Jones (LJ) potential $U_{\mathrm{LJ}}(r_{ij}) = 4\varepsilon\left[(\sigma/r_{ij})^{12} - (\sigma/r_{ij})^{6}\right]$ where r_{ij} is the distance between atoms i and j, ε is the energy scale, and σ is the length scale. The LJ potential is strongly anharmonic, which induces inelastic phonon processes. In order to suppress inelastic phonon processes in certain regions, we replace the LJ potential with its second-order Taylor expansion about the equilibrium separation $r_{\mathrm{eq}} = 2^{1/6}\sigma$, $U_{\mathrm{harmonic}}(r_{ij}) = \frac{1}{2}k(r_{ij} - r_{\mathrm{eq}})^2$, where $k = 36(2)^{2/3}\varepsilon/\sigma^2$. In all simulations, atoms interact only with their nearest

neighbors, which is a difference from other MD work. This was enforced for both LJ and harmonic potentials and for both intra-species and cross-species interactions. The main reason is that, since the harmonic potential does not tend to zero as $r_{ij} \to \infty$, it is ill suited to describe the forces of more distant neighbors. We limit the interactions within both potentials to include nearest neighbors only so that U_{harmonic} approximates U_{LJ} in a straightforward manner. This also precludes cross-species interactions beyond those between the two immediate monolayers, which would be ordinarily present using the standard LJ potential and would introduce additional complexity to the comparison between harmonic and anharmonic systems.

We have calculated the interfacial thermal conductance in systems with four different configurations of these forces: (a) all LJ, (b) all LJ except with harmonic interactions across the interface, (c) all harmonic except with LJ interface, and (d) all harmonic. Examples of steady-state temperature profiles from all four cases under otherwise identical simulation conditions are shown in Fig. 1. Each data point represents the average temperature in each bin as described in Appendix A, and the shaded region indicates the 95% prediction interval for the bin temperatures. We note that the temperature profiles in cases (c) and (d) have effectively zero slope, corresponding to the diverging conductivity expected in a material with no phonon–phonon scattering.

In order to calculate the interfacial thermal conductance from each simulation, the temperatures in the bulk leads are fitted to a linear profile and extrapolated to the interface, which allows the definition of the temperature drop ΔT.[25] The conductance is then

$$h = \frac{\dot{Q}}{A\,\Delta T}, \tag{1}$$

where A is the cross-sectional area and $\dot{Q}$ is the steady heat current added to the heat source and removed from the heat sink. Ten such simulations were performed in each system at each temperature with randomized initial velocities to provide independent trials. The mean conductance values from those trials are plotted in Fig. 2 with error bars indicating 95% confidence intervals.

The conductances in all four systems converge at low temperatures, since displacements are small and the LJ potential is well approximated by the harmonic potential. As temperature increases, the conductance increases in case (a), as has been observed in MD simulations in previous work.[5–7] The conductance also increases with temperature in cases (b) and (c), although at smaller rates. In contrast, the conductance in the harmonic case (d) is constant with temperature. These results are consistent with the hypothesis that, in the classical limit, increasing conductance with temperature is caused by inelastic processes, which are enabled by anharmonicity. The average

and standard deviation of these values is 24.9 ± 0.8 MW m^{-2} K^{-1}. Empirically, we note that adding the "excess" conductance from cases (b) and (c) to the harmonic case (d) at each temperature produces conductance values (gray dashed line) very similar to those obtained in the all-LJ case (a). This lends support to the notion that the anharmonic contributions from the interface and from the bulk regions are simply additive.

For comparison, we have also calculated the conductance of the harmonic system using atomistic Green's functions (AGF) to model both a two-probe[26] and a four-probe measurement.[27] The two respective conductance values are 21.69 MW m^{-2} K^{-1} and 26.69 MW m^{-2} K^{-1}, converged within 0.01 MW m^{-2} K^{-1} with respect to wavevector and frequency sampling. Details of these calculations are given in Appendix B. The conductance obtained by NEMD in the harmonic system falls between the predictions of the two AGF models and in somewhat closer agreement with the four-probe model. This is consistent with the fact that the four-probe model better describes the physical circumstances of the NEMD calculation, in which the conductance is calculated based on temperatures extrapolated to the interface rather than the temperatures at the baths. Physically, the NEMD conductance is also expected to be slightly higher than the two-probe conductance. The difference is apparent in the temperature profile of the harmonic system in Fig. 1(d); small contact resistances between the hot/cold baths and the Ar/heavy-Ar leads cause the temperature difference at the interface to be slightly smaller than that between the baths. By calculating conductances using bath temperatures from the NEMD simulations, the effective conductance in the harmonic system is 22.3 ± 2.6 MW m^{-2} K^{-1} in closer agreement with the two-probe prediction, as shown in Appendix A. These comparisons corroborate the NEMD results and provide evidence that they are free of serious size and edge effects as cautioned in other work,[28,29] since AGF calculations do not suffer from the same issues.

The key observation from Fig. 2 is that the system consisting of LJ solids joined by harmonic interfacial forces [case (b)] exhibits a consistently higher conductance than the system of harmonic solids joined by LJ forces [case (c)]. Moreover, the discrepancy grows with temperature. We therefore conclude that, in this system, inelastic phonon processes in the bulk materials make a larger contribution to the conductance than inelastic processes at the interface.

III. ROLE OF BULK INELASTIC SCATTERING

In this section, we present calculations of the energy distributions among the normal modes in the same NEMD simulations described in the previous section. By comparing the energy distributions, we elucidate the phonon phenomena that are responsible for the differences in conductance observed in Section II. We use the wavelet transform, which has been applied previously to analyze the distribution of energy in MD simulations in spatial and spectral domains simultaneously.[30] To collect the signal to be transformed, we sampled atomic velocities every 40 ns during the same period in which the temperature profiles were collected. We chose to sample normal modes with wavevector $\mathbf{q}$ parallel to the $\langle 001 \rangle$ direction; therefore, we obtained the average velocity $\bar{\mathbf{v}}$ of atoms in each monolayer (i.e., each (002) plane) to form a one-dimensional signal $w_\alpha(z) = \sqrt{m(z)/2}\,\bar{v}_\alpha(z)$ corresponding to each Cartesian component α. The wavelet transform of that signal, $\tilde{w}(z',q')$, is then used to calculate a kinetic energy density $E^{\mathrm{K}}(z,q)$ as a function of both space and wavenumber. For ease of interpretation, we convert this to an equivalent temperature, $T_{\mathrm{equiv}}(z,q)$; i.e., the temperature of a classical system at thermal equilibrium with an equal energy density. In principle, the same procedure can also be used to obtain the spectra of modes in directions other than (001) by sampling the corresponding planar velocities. However, the geometry of the system introduces complications in the interpretation of spectra in off-axis directions, so we present spectra along (001) only. For brevity, we also present only the spectra corresponding to longitudinal polarization. We find that the spectra corresponding to transverse modes are very similar because, although their frequencies differ from the longitudinal modes, mode conversion does not occur at sharp interfaces for wavevectors along $\langle 001 \rangle$,[31] and the wavenumber of the transverse Ar modes corresponding to the cutoff frequency of the transverse heavy Ar modes is the same. Further details regarding this calculation are given in Appendix C.

The resulting kinetic energy densities from six sets of NEMD simulations are plotted in Fig. 3. To reduce noise, the energy density shown in each panel is obtained from averaging data from ten simulations. Each paired row of panels is taken at the same temperature, increasing from top to bottom: (a, b) 2 K, (c, d) 26 K, and (e, f) 50 K. In each pair, the left panel is from the all-LJ system, and the right panel is from the all-harmonic system. In each system, the average spectral temperature decreases from left to right, reflecting the decrease in total temperature. The sharp decrease at $z = 0$ reflects the temperature discontinuity at the interface. Since the simulations are classical, the energy density at thermal equilibrium would exhibit a uniform distribution among

wavevectors (i.e., along vertical sections). The color scales are chosen proportionally to the total temperature so that relative deviations from the equilibrium distribution can be compared at different temperatures.

Interestingly, the energy distribution is in significant nonequilibrium on the Ar side in the LJ system at low temperature [panel (a)] and in the harmonic system at all temperatures [panels (b, d, f)]. There is excess energy in the modes with wavenumbers above $q \approx 0.4 q_{\mathrm{max}}$, while there is a deficit of energy at lower wavenumbers. The threshold coincides with the wavenumber of the Ar mode that has the same frequency as the cutoff frequency of heavy Ar, $q/q_{\mathrm{max}} = 2\pi^{-1} \sin^{-1}(m_{\mathrm{Ar}}/m_{\mathrm{h\text{-}Ar}})$. Therefore, we attribute the nonequilibrium to the fact that, in the harmonic system and in the low-temperature LJ system, phonons can only transmit elastically at the interface. High-frequency phonons originating in the Ar are therefore completely reflected at the interface, since there are no available modes of the same frequency in the heavy Ar.

As temperature increases in the LJ system, the atomic displacements increase, and the anharmonic forces enable the exchange of energy among modes of different frequency—i.e., the rates of inelastic processes increase. This leads to thermalization of vibrational energy in the Ar in the sequence from panel (a) to (c) to (e): the energy that is confined above $q/q_{\mathrm{max}} \approx 0.4$ steadily relaxes into modes below the threshold. In light of the results of Section II, this thermalization correlates with a drastic increase in thermal conductance of the interface. We therefore infer that conductance increases due to an increasing rate of thermalization of excess energy in high-frequency, non-transmitting modes to low-frequency modes with a high transmission.

The kinetic energy spectra of the remaining two types of systems are shown in Fig. 4: the left panels are from LJ systems with harmonic interfacial forces, and the right panels are from harmonic systems with LJ interfacial forces. In other words, the systems differ from those of Fig. 3 only in the forces at the interface. The energy distributions of corresponding panels look remarkably similar, which implies that the interfacial forces have only a minor effect on the thermalization of modes in the Ar. In particular, we note that the LJ forces at the interface between harmonic solids only promotes thermalization very weakly if at all. This is associated with a relatively small increase in conductance with temperature in case (c) of Fig. 2, which we attribute to the bona fide interfacial inelastic phonon processes investigated in detail by Sääskilahti et al.[7]

IV. CONCLUSIONS

We have used classical molecular dynamics simulations to investigate the contributions to interfacial thermal conductance from anharmonic effects at the interface and in the nearby bulk materials. First, we confirmed that anharmonicity of interatomic forces is responsible for the increase of conductance with temperature. The results support the physically appealing model that the total thermal conductance at an interface is the sum of a contribution from elastic phonon transmission (which is constant in the classical limit) and a contribution from inelastic phonon processes that increases with temperature. We found that the inelastic part of the conductance can be further decomposed into contributions from bulk inelastic and interfacial inelastic processes. Between the two, the contribution from bulk inelastic processes is larger than that from the interface itself, and this difference grows with temperature. We then used the wavelet transform to obtain kinetic energy spectra, which show energy distributions exhibiting strong non-equilibrium at low temperatures because transmission is purely elastic. As temperature increases, the energy distribution in the anharmonic system approaches a thermal distribution, presumably due to an increase in bulk scattering rates. We hypothesize that this increase in bulk scattering enables an increasing contribution to the interfacial flux from non-transmitting modes, and that this mechanism is responsible for the majority of the observed increase in conductance with temperature. The same thermalization is not observed in a system with anharmonic forces only at the interface and harmonic forces elsewhere, suggesting that purely interfacial inelastic scattering contributes to increased conductance through a different mechanism, such as directly increasing the effective transmission, as observed in previous work.[7] In addition to improving the understanding at single interfaces, the identification of these separate types of contributions from inelastic processes will also be useful in understanding the role of anharmonicity at interfaces incorporating thin layers for thermal engineering, which we are also investigating in other work.[32]

The present conclusions apply strictly to the Ar/heavy-Ar interface, which has been used extensively as a model system for interfacial thermal conductance. There are some aspects that should be investigated further to extend the findings to other systems, such as metal/diamond interfaces that have been measured experimentally. The present work does not address the effects of interfacial disorder or lattice mismatch, which may play important roles in the experimental systems. Furthermore, the vibrational mismatch of the Pb/diamond interface, for example, is much larger than the mismatch of the Ar/heavy-Ar system studied in this and most other MD work on this

problem. Gordiz and Henry did recently investigate the effects of increasing mismatch explicitly, and showed that the anharmonic contribution to conductance becomes particularly important at large mismatch in bonding strength.[33]

Nevertheless, the present findings provide important general guidance for the development of interfacial thermal conductance models that can accurately incorporate inelastic processes. Namely, our results suggest that it is not sufficient for conductance models to account only for frequency conversion at the interface, as done e.g. in the HHIM[20] and the AIM.[21] In addition, it is necessary to account for the effective increase of incident phonon flux due to rethermalization of energy in modes with low transmission, as was done phenomenologically, for example, by Duda et al.[22] New models that incorporate these effects could take the parameters of the Ar/heavy-Ar system as input and test their predictions directly against the conductance contributions from elastic, bulk inelastic, and interfacial inelastic processes provided in this work.

ACKNOWLEDGMENTS

N.Q.L., R.R., and P.M.N. acknowledge the financial support of the Air Force Office of Scientific Research (FA9550-14-1-0395). C.A.P., J.Z., and A.W.G. acknowledge financial support from NSF-CAREER (QMHP 1028883) and NSF-IDR (CBET 1134311). Computational work was performed using resources of the Advanced Research Computing Services at the University of Virginia and the Extreme Science and Engineering Discovery Environment (XSEDE) (DMR130123) supported by National Science Foundation (ACI-1053575). The authors are grateful for useful discussions with C.H. Baker, P.E. Hopkins, and A.J.H. McGaughey.

Appendix A: Ar/heavy Ar simulation details

All molecular dynamics simulations were performed with the LAMMPS code package.[34] In choosing the model system, we sought the simplest system in which one can observe the effect of anharmonicity on thermal conductance and on phonon transport. A system meeting these criteria, similar to systems used in past MD studies of interfacial conductance,[5,7,25] is a coherent [001] interface between solid Ar (40 amu) and solid "heavy Ar" (120 amu). In this work, we use the LJ parameters $\varepsilon = 0.01617$ eV and $\sigma = 3.347$ Å, which correspond to the harmonic parameters $k = 0.8249$ eV Å^{-2} and $r_{eq} = 3.757$ Å.

These interatomic potentials produce a cubic lattice parameter of 5.313 Å at 0 K, compared with 5.311 Å extrapolated for Ar from experimental data.[35] The potentials produce phonon dispersions in good agreement with neutron scattering measurements in solid Ar,[36] as shown in Fig. 5. The highest-frequency mode has a vibrational period of 500 fs, based on which we select a timestep of 2 fs. To account for thermal expansion in the systems with LJ forces, simulations were performed to determine the zero-pressure lattice constant as a function of temperature. The simulations produced values of $a(T)$ that were fitted to a third-order polynomial function

$$a(T) = a_0 + a_1 T + a_2 T^2 + a_3 T^3. \tag{A1}$$

The fitted coefficients are provided in Table I.

The NEMD simulation domain has dimensions of $10 \times 10 \times 60$ conventional unit cells. The boundary conditions are periodic in the plane of the interface, approximating the interface between two slabs of infinite cross section. On each end, two (002) planes are held fixed as walls (400 atoms), and the temperature of the next twenty (002) planes (4000 atoms) is controlled using a Langevin thermostat with a time constant of 2.14 ps. Sääskilahti et al.[7] determined that this geometry was sufficiently large to avoid size effects in their system. In NEMD of harmonic and low-temperature systems, energy outgoing from the interface must be well thermalized in the two thermostatted regions ("baths") so that the distribution of energy emitted from each bath is in thermal equilibrium. Insufficient thermalization manifests as a dependence of thermal properties on system size, thermostat strength, or size of the bath. Since (1) the forces in some of our systems are purely harmonic and (2) our LJ potential is limited to nearest-neighbor interactions, presumably reducing phonon–phonon scattering even in our anharmonic systems, we performed additional simulations to check for evidence of insufficient thermalization of phonons emitted from the baths. Namely, we ran three series of simulations with increased cross-section (15×15 cells), increased length (90 cells), and decreased thermostat time constants (1.07 and 0.54 ps) with no statistically significant change in conductance, suggesting that the Langevin thermostats provide sufficient thermalization to avoid size and edge effects as others have cautioned.[28,29] This is also supported by the fact that the conductance also falls between the values predicted by two complementary AGF methods (Section II and Appendix B), in which the distributions of energy emitted from the temperature baths are prescribed exactly and are not coupled with the distributions of energy leaving the interface.

Each simulation began with the atoms in their equilibrium positions and with kinetic energy

equivalent to twice the nominal temperature. For simplicity, the initial atomic velocities were set to the corresponding uniform magnitude of $|\mathbf{v}| = (2dk_{\mathrm{B}}T_{\mathrm{nominal}}/m)^{1/2}$ with random orientation. The simulation then ran for 20 ps in order to reach thermal equilibrium. The thermostats were then applied at target temperatures of $(1 \pm 1/10)T_{\mathrm{nominal}}$ for 4 ns, at which point we confirmed that the temperature distributions had reached steady state. To determine the temperature distribution, we divided the atoms into 120 bins along the transport direction, each bin containing one monolayer (200 atoms). The temperature was sampled in each bin in intervals of 1 ps. Running averages were stored in memory and written to disk every 40 ps, and those averages were collected for 8 ns, which provided 200 samples of the temperature in each bin. To check the degree to which the LJ systems at different temperatures are approximated by the harmonic system, we have also calculated distributions of atomic displacements from equilibrium during the NEMD simulations. Distributions from six selected simulations are shown in Fig. 6. At 2 K, the distributions are nearly identical, and the distributions increasingly diverge with increasing temperature.

Each simulation thus provided a one-dimensional temperature distribution $T(z)$. We used a standard procedure for extracting the thermal conductance at the interface: we fit a linear model to the temperature profiles in the two "bulk-like" regions and extrapolated them to the interface.[25] We calculated ΔT as the difference between the extrapolated values, from which we calculated the conductance using Eq. (1). In Section II, we comment that in the special case of the harmonic system, replacing the extrapolated temperatures with the temperatures of the thermostatted regions enables a fair comparison with the two-probe conductance model using atomistic Green's functions (AGF). Those data are shown in Fig. 7 (blue circles) in comparison with the conductance calculated using the extrapolated temperatures (red crosses) and the AGF value (gray line). The inclusion of the contact resistances appears to be a plausible explanation for the discrepancy between the methods.

Appendix B: Atomistic Green's Functions

According to the formalism of atomistic Green's functions (AGF) in the harmonic limit, the thermal conductance of a "device" (in this case, a single planar interface between two materials) in contact with reservoirs at thermal equilibrium is given by[37,38]

$$h_{2\mathrm{p}} = \frac{1}{2\pi A}\int_0^\infty \hbar\omega \frac{\partial N}{\partial T}\mathrm{Tr}\left\{\Gamma_l G \Gamma_r G^\dagger\right\} d\omega, \tag{B1}$$

where A is the cross-sectional area, $\hbar\omega$ is the phonon energy, N is the Bose–Einstein distribution, and T is the temperature. G is the retarded Green's function for the dynamical equation of the device, which describes the response of the device upon an impulse excitation. Γ_l (Γ_r) is the anti-Hermitian part of the left (right) contact self-energy. This quantity is related to the rate at which phonons leak from the device into the left (right) contact.[38] Equation B1 corresponds to a two-probe measurement based on the temperatures of phonons emitted from the reservoirs, which exhibit an equilibrium distribution. A modification has been proposed to approximate a four-probe measurement based on the combined energy density of phonons emitted from the reservoirs and those transmitted through the interface:[27]

$$h_{4\mathrm{p}} = h_{2\mathrm{p}} \frac{1}{1 - \frac{1}{2}\left[\frac{h_{2\mathrm{p}}}{h_l} + \frac{h_{2\mathrm{p}}}{h_r}\right]}, \tag{B2}$$

where h_l and h_r are the effective conductances of the pure materials. Detailed explanations of the AGF method and its numerical implementation are available in the literature;[27,37–41] here we discuss details relevant to the present systems.

To compare the conductances calculated from AGF and classical MD simulations, we evaluate Eqs. B1 and B2 in the classical limit ($\hbar\omega \ll k_{\mathrm{B}}T$). In that limit, the factor $\hbar\omega(\partial N/\partial T)$ reduces to the Boltzmann constant, k_{B}, and the thermal conductance becomes

$$h = \frac{k_{\mathrm{B}}}{2\pi A} \int_0^\infty \mathrm{Tr}\left\{\Gamma_l G \Gamma_r G^\dagger\right\} d\omega. \tag{B3}$$

We used AGF to calculate the conductance at the Ar/heavy-Ar interface in the harmonic limit. The interatomic force constants were calculated from the Taylor expansion of the total energy, and we verified that they produce the same spectrum of normal modes. To calculate $\mathrm{Tr}\left\{\Gamma_l G \Gamma_r G^\dagger\right\}$, we use the transverse symmetry of the system to decompose the problem into a sum of independent systems in the transverse k-space.[42] The transverse Brillouin zone was sampled with a grid of 200×200 equally spaced k-points.

Appendix C: The wavelet transform

The wavelet transform $\tilde{w}(q,z)$ of a signal $w(z)$ is an integral transform,

$$\tilde{w}(z',q') = \mathscr{W}\{w(z)\} = \int_{-\infty}^{\infty} w(z)\, \psi^*_{z',q'}(z)\, dz, \tag{C1}$$

where the kernel functions $\psi_{z',q'}$ are wavelets. We use the convention of Baker et al.[30] in which each "daughter wavelet," corresponding to a specific location z' and wavenumber q', is defined as

$$\psi_{z',q'}(z) = \pi^{-1/4}\left(\frac{q'}{q_0}\right)^{1/2}\exp\left[iq'(z-z')\right]\times \exp\left[-\frac{1}{2}\left(\frac{q'}{q_0}\right)^2(z-z')^2\right]. \tag{C2}$$

This is a scaled and translated version of a mother wavelet ψ_{z',q_0} whose dominant wavenumber is q_0. The definition is normalized so that the energy density per length, per wavenumber is calculated as

$$E_\psi(z',q') = \frac{1}{Cq_0}|\tilde{w}(z',q')|^2. \tag{C3}$$

We use the combination $w(z) = \sqrt{m(z)/2}\,v(z)$ as the signal to be transformed so that the wavelet energy density calculated by Eq. (C3) corresponds to the density of kinetic energy per length, per wavenumber. The constant C accounts for the fact that, unlike the plane waves that form the basis functions for the Fourier transform, the wavelets are not orthogonal:

$$C = \int_{-\infty}^{\infty}\frac{|\bar{\psi}_{z',q_0}(q)|^2}{|q|}dq, \tag{C4}$$

where $\bar{\psi}_{z',q_0'}(q)$ is the Fourier spectrum of the mother wavelet.

The window of useful information from the spectrum is bounded in wavenumber space from above due to aliasing artifacts at short wavelengths and from below due to edge artifacts at long wavelengths. We use the tolerances for these artifacts suggested in Ref. 30, corresponding respectively to constants $\eta = 0.05$ and $\phi = 1$ defined therein. Based on those constraints, one may choose the dominant wavenumber of the mother wavelet, q_0, to determine the range of useful information in the final spectrum. In this work, we used $q_0 = 10/a$, which produces an energy spectrum with useful information in the range of wavenumbers between $q_{\text{low}} \approx 0.19q_{\text{max}}$ and $q_{\text{high}} \approx 0.83q_{\text{max}}$. These correspond to the limits on the vertical axes in Figs. 3 and 4 and allow a clear representation of changes in the energy distribution occurring near $0.4q_{\text{max}}$.

To facilitate interpretation, the values plotted in those figures are not $E(z,q)$ itself, but rather the equivalent temperature

$$T_{\text{equiv}}(z,q) = \frac{2L_z(q_{\text{high}}-q_{\text{low}})}{k_{\text{B}}}E(z,q), \tag{C5}$$

where L_z is the system length in the z direction. That is, if a system were at thermal equilibrium with a uniform energy density of $E(z,q)$, then its temperature would be equal to $T_{\text{equiv}}(z,q)$.

---

* nql6u@virginia.edu; Present Address: US Naval Research Laboratory, Washington, DC 20375

† pamela@virginia.edu

[1] R. J. Stoner, H. J. Maris, T. R. Anthony, and W. F. Banholzer, Physical Review Letters **68**, 1563 (1992).

[2] R. J. Stoner and H. J. Maris, Physical Review B **48**, 16373 (1993).

[3] H. K. Lyeo and D. G. Cahill, Physical Review B **73**, 144301 (2006).

[4] G. T. Hohensee, R. B. Wilson, and D. G. Cahill, Nature Communications **6**, 6578 (2015).

[5] R. J. Stevens, L. V. Zhigilei, and P. M. Norris, International Journal of Heat and Mass Transfer **50**, 3977 (2007).

[6] E. S. Landry and A. J. H. McGaughey, Physical Review B **80**, 165304 (2009).

[7] K. Sääskilahti, J. Oksanen, J. Tulkki, and S. Volz, Physical Review B **90**, 134312 (2014).

[8] A. Sarua, H. Ji, K. P. Hilton, D. J. Wallis, M. J. Uren, T. Martin, and M. Kuball, IEEE Transactions on Electron Devices **54**, 3152 (2007).

[9] J. Kuzmík, S. Bychikhin, D. Pogany, C. Gaquière, E. Pichonat, and E. Morvan, Journal of Applied Physics **101**, 054508 (2007).

[10] U. K. Mishra, L. Shen, T. E. Kazior, and Y.-F. Wu, Proceedings of the IEEE **96**, 287 (2008).

[11] I. M. Khalatnikov, Zhurnal Eksperimental'noi i Teoreticheskoi Fiziki **22**, 687 (1952).

[12] W. A. Little, Canadian Journal of Physics **37**, 334 (1959).

[13] E. T. Swartz and R. O. Pohl, Applied Physics Letters **51**, 2200 (1987).

[14] E. T. Swartz and R. O. Pohl, Reviews of Modern Physics **61**, 605 (1989).

[15] R. J. Stevens, A. N. Smith, and P. M. Norris, Journal of Heat Transfer **127**, 315 (2005).

[16] B. N. Brockhouse, T. Arase, G. Caglioti, K. R. Rao, and A. D. B. Woods, Physical Review **128**, 1099 (1962).

[17] J. L. Warren, J. L. Yarnell, G. Dolling, and R. A. Cowley, Physical Review **158**, 805 (1967).

[18] Y. A. Kosevich, Physical Review B **52**, 1017 (1995).

[19] P. E. Hopkins and P. M. Norris, Nanoscale and Microscale Thermophysical Engineering **11**, 247 (2007).

[20] P. E. Hopkins, Journal of Applied Physics **106**, 013528 (2009).

[21] P. E. Hopkins, J. C. Duda, and P. M. Norris, Journal of Heat Transfer **133**, 062401 (2011).

[22] J. C. Duda, P. M. Norris, and P. E. Hopkins, Journal of Heat Transfer **133**, 074501 (2011).

[23] X. Wu and T. Luo, Journal of Applied Physics **115**, 014901 (2014).

[24] T. Murakami, T. Hori, T. Shiga, and J. Shiomi, Applied Physics Express **7**, 121801 (2014).

[25] T. S. English, J. C. Duda, J. L. Smoyer, D. A. Jordan, P. M. Norris, and L. V. Zhigilei, Physical Review B **85**, 035438 (2012).

[26] N. Mingo and L. Yang, Physical Review B **68**, 245406 (2003).

[27] Z. Tian, K. Esfarjani, and G. Chen, Physical Review B **86**, 235304 (2012).

[28] R. E. Jones, J. C. Duda, X. W. Zhou, C. J. Kimmer, and P. E. Hopkins, Applied Physics Letters **102**, 183119 (2013).

[29] Z. Liang and P. Keblinski, Physical Review B **90**, 075411 (2014).

[30] C. H. Baker, D. A. Jordan, and P. M. Norris, Physical Review B **86**, 104306 (2012).

[31] P. K. Schelling, S. R. Phillpot, and P. Keblinski, Applied Physics Letters **80**, 2484 (2002).

[32] C. A. Polanco, R. Rastgarkafshgarkolaei, J. Zhang, N. Q. Le, P. M. Norris, and A. W. Ghosh, Physical Review B **95**, 195303 (2017).

[33] K. Gordiz and A. Henry, Scientifc Reports **5**, 18361 (2015).

[34] S. Plimpton, Journal of Computational Physics **117**, 1 (1995), code available at `lammps.sandia.gov`.

[35] O. G. Peterson, D. N. Batchelder, and R. O. Simmons, Physical Review **150**, 703 (1966).

[36] D. N. Batchelder, M. F. Collins, B. C. G. Haywood, and G. R. Sidey, Journal of Physics C: Solid State Physics **3**, 249 (1970).

[37] N. Mingo and L. Yang, Phys. Rev. B **68**, 245406 (2003).

[38] S. Datta, *Quantum Transport: Atom to Transistor*, 2nd ed. (Cambridge University Press, 2005).

[39] W. Zhang, T. S. Fisher, and N. Mingo, Numerical Heat Transfer, Part B: Fundamentals **51**, 333 (2007).

[40] J.-S. Wang, J. Wang, and J. T. L?, The European Physical Journal B **62**, 381 (2008).

[41] P. E. Hopkins, P. M. Norris, M. S. Tsegaye, and A. W. Ghosh, Journal of Applied Physics **106**, 063503 (2009).

[42] W. Zhang, T. S. Fisher, and N. Mingo, Journal of Heat Transfer **129**, 483 (2006).

452 **FIGURES**

453

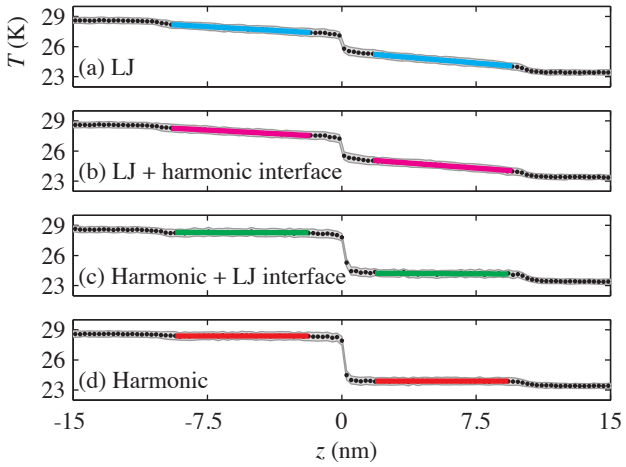

454

455 FIG. 1. Steady-state temperature profiles in four identical systems except for the anharmonicity of the
456 interatomic forces. The nominal temperature of these simulations is $T = 26$ K.

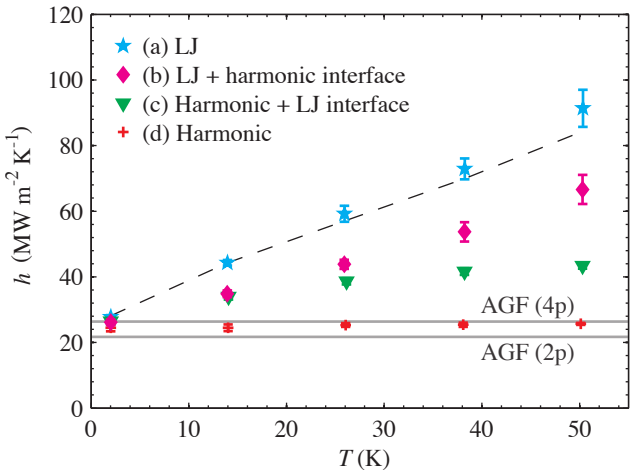

FIG. 2. Thermal boundary conductance as a function of temperature in the same systems as in Fig. 1. Also shown are conductance values calculated using atomistic Green's functions to model two-probe and four-probe measurements (solid gray). The dashed gray line is the sum of the harmonic conductance of case (d) with the "excess" conductances from cases (b) and (c).

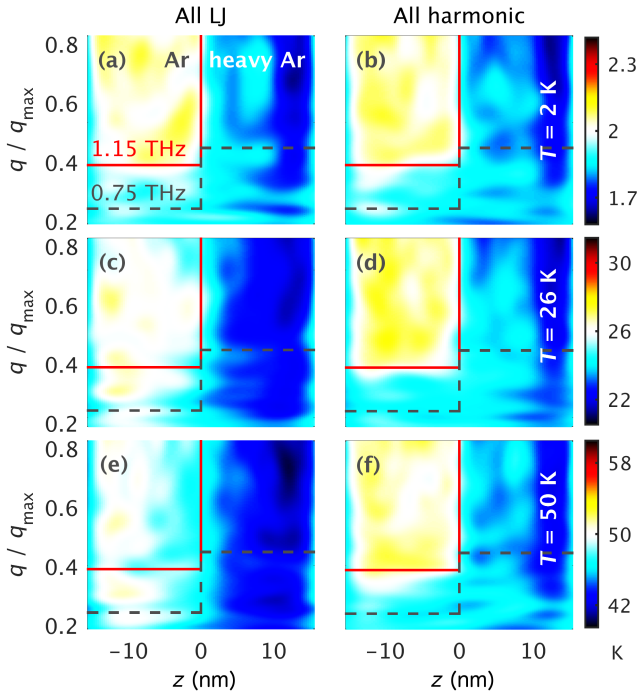

462

463 FIG. 3. Distributions of kinetic energy in longitudinal ⟨001⟩ modes obtained by a wavelet transform during
464 NEMD simulations between Ar ($z < 0$) and heavy Ar ($z > 0$). Modes with frequency 0.75 THz are marked
465 with dashed gray lines; modes with frequency 1.15 THz, the maximum frequency in heavy Ar, are marked
466 in solid red. The nominal temperature increases from top to bottom: (a, b) 2 K, (c, d) 26 K, and (e, f) 50 K.
467 The left panels (a, c, e) are calculated from systems with all LJ forces and the right panels (b, d, f) from
468 systems with all harmonic forces.

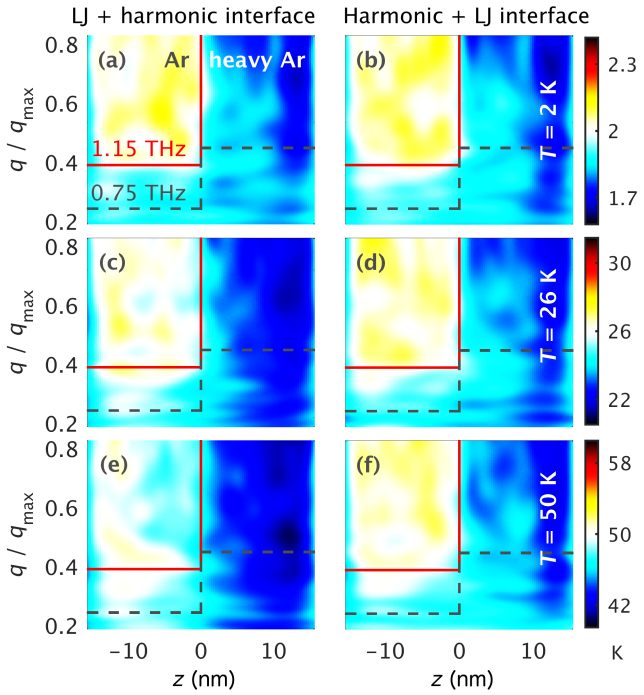

469

470 FIG. 4. The same as Fig. 3, but with different forces between atoms at the interfaces. The left panels (a, c,
471 e) are calculated from LJ systems with harmonic interfacial forces, and the right panels (b, d, f) are from
472 harmonic systems with LJ interfacial forces.

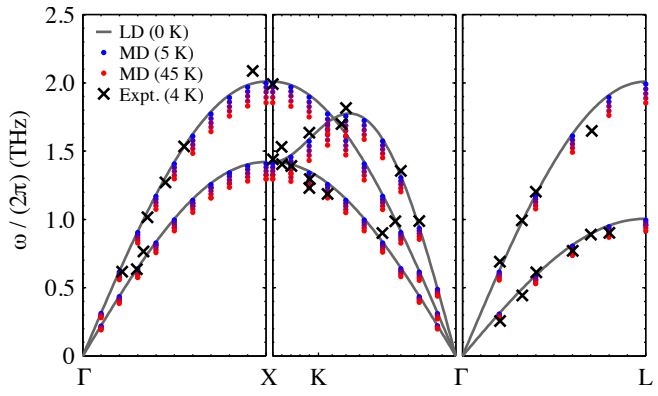

FIG. 5. Dispersion of normal modes in simulated argon from lattice dynamics (LD) and from normal mode decomposition from molecular dynamics simulations (MD) compared with experimental measurements from Ref. 36.

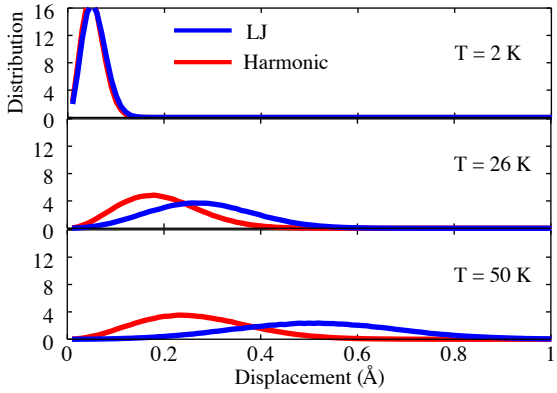

FIG. 6. Average displacements of Ar atoms from their equilbrium positions during NEMD simulations used to calculate conductances in Fig. 2. Distributions were calculated from atoms within the twelve monolayers nearest the interface in six simulations: one simulation with all LJ forces (blue) and one with all harmonic forces (red) at each of three temperatures: 2 (top), 26 (center), and 50 K (bottom).

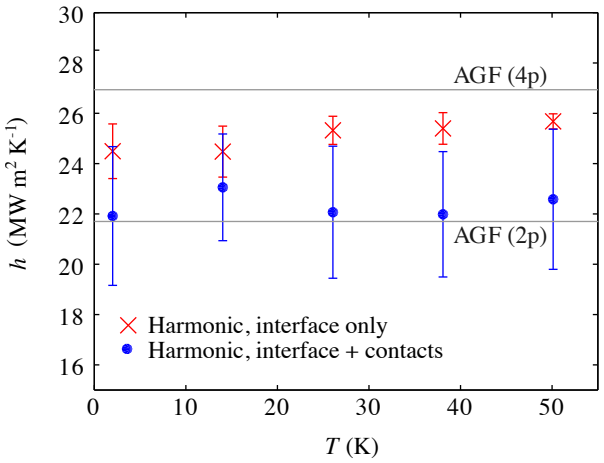

FIG. 7. Conductance in the harmonic system calculated from NEMD using the lead temperatures extrapolated to the interface (red crosses) and the bath temperatures (blue circles) compared with two-probe (2p) and four-probe (4p) AGF calculations.

TABLES

TABLE I. Coefficients for Temperature-Dependent Lattice Parameter of LJ Argon [Eq. (A1)]

Parameter	Fitted Value
a_0	5.313 Å
a_1	1.813×10^{-3} Å K^{-1}
a_2	4.792×10^{-6} Å K^{-2}
a_3	1.394×10^{-8} Å K^{-3}